DFT Study of Hydrostatic Pressure Effects up to 1.0 GPa on the Electronic and Magnetic Properties of Laves Phases $ErAl_2$ and $ErNi_2$

T. López-Solenzal , J.L. Sanchez Llamazares , J.L. Enríquez-Carrejo , C.F. Sánchez-Valdés *

Posted Date: 12 May 2025

doi: 10.20944/preprints202505.0871.v1

Keywords: density functional theory calculations; Laves phases; electronic structure; magnetic properties; hydrostatic pressure

 doi:10.20944/preprints202505.0871.v1

Article

DFT Study of Hydrostatic Pressure Effects up to 1.0 GPa on the Electronic and Magnetic Properties of Laves Phases $ErAl_2$ and $ErNi_2$

T. López-Solenzal [1], J.L. Sánchez Llamazares [2], J.L. Enríquez-Carrejo [1] and C.F. Sánchez-Valdés [1,*]

[1] Departamento de Física y Matemáticas, Extensión Multidisciplinaria en Ciudad Universitaria, Instituto de Ingeniería y Tecnología, Universidad Autónoma de Ciudad Juárez, Ciudad Juárez, Chihuahua 32310, México

[2] Instituto Potosino de Investigación Científica y Tecnológica A.C., Camino a la Presa San José 2055, Col. Lomas 4ª, San Luis Potosí, S.L.P. 78216, México

* Correspondence: cesar.sanchez@uacj.mx; Tel.: +53 656-688-2100

Abstract: This study employs DFT+U calculations to investigate the ferromagnetic properties of $ErAl_2$ and $ErNi_2$ Laves phases under an external hydrostatic pressure P (0 GPa ≤ P ≤ 1.0 GPa). The calculated magnetic moments per formula unit for both crystalline structures align with experimentally reported values: 4.40 μ_B/f.u. in the hard magnetization <001> axis for $ErAl_2$ and 5.56 μ_B/f.u. in the easy magnetization <001> axis for $ErNi_2$. The DFT results indicate that the magnetic moment remains unchanged up to 1 GPa of hydrostatic pressure, with no structural instabilities observed, as evidenced by a nearly constant formation energy for $ErAl_2$ and $ErNi_2$ alloys. The simulations confirm that the magnetic behavior of $ErAl_2$ is primarily driven by the electrons localized in the f orbitals. In contrast, for $ErNi_2$, both d and f orbitals significantly contribute to the total magnetic moment. Finally, the electronic specific heat coefficient was calculated and reported as a function of hydrostatic pressure up to P = 1.0 GPa for each Laves phase.

Keywords: density functional theory calculations; Laves phases; electronic structure; magnetic properties; hydrostatic pressure

1. Introduction

A renewed interest has recently emerged in studying rare-earth-based Laves phases due to their excellent magnetocaloric properties, which make them suitable as magnetic refrigerants for hydrogen magnetocaloric liquefaction [1–9]. This solid-state cooling technology is environmentally friendly and more energy-efficient than conventional refrigeration methods that rely on the Joule-Thomson effect [1,3,6–9].

In stoichiometric AB_2-type rare-earth-based Laves phases, A represents the rare earth element, while B denotes a transition or post-transition metal. The relative ratio of elements A and B, r_A/r_B, ranges from 1.05 to 1.68, with a higher packing density achieved at an ideal atomic radius ratio of 1.225, which corresponds to a space-filling of 71 % in the crystal structure [10,11]. Rare-earth-based Laves phases exhibit three typical crystal structures known as C15 (cubic), C14 (hexagonal), and C36 (hexagonal).

The present work examines the effect of hydrostatic pressure on the electronic structure and magnetic properties of the ferromagnetic ErM_2 compounds, where M is either Al or Ni. These compounds crystallize into a $MgCu_2$-type cubic structure (C15) [12–14], with lattice parameters *a* of 7.770 Å and 7.113 Å, respectively [15,16]. The $MgCu_2$-type crystal structure exhibits a valence electron concentration per atom (e/a) of less than 1.8 (i.e., e/a < 1.8), which contributes to the stability of the C15-type Laves phases. $ErAl_2$ and $ErNi_2$ display ferromagnetic order, with Curie temperatures (T_C) of 12.5 K and 6.8 K, respectively [15,16]. They have r_A/r_B ratios of r_{Er}/r_{Al} = 1.245 and r_{Er}/r_{Ni} = 1.162. The

 doi:10.20944/preprints202505.0871.v1

total magnetic moment per formula unit in both compounds originates from the rare earth element (Er), which possesses unpaired electrons [10,11,17].

Ab initio calculations employing density-functional theory (DFT) are essential tools for investigating the relationship between electronic structure and the physicochemical properties of materials [18]. In this study, these calculations have been utilized to examine the correlation between electronic structures and the magnetic properties of the two previously mentioned ferromagnetically ordered compounds [17,19–24]. The application of first-principles methods for computing electronic structures and performing energy calculations to address the inherent challenges of Laves phase investigations is an emerging field [25].

In this work, we examine the effect of hydrostatic pressure on the electronic structure and magnetic properties of the ferromagnetically ordered $ErAl_2$ and $ErNi_2$ Laves phases along the <001> direction using the spin-polarized DFT+U method with Hubbard U potential. We highlight the role of the Al and Ni orbitals in the electronic structure. To our knowledge, no in-depth investigations have used DFT methods to analyze the magnetic properties along the <001> axis in these two Laves phases. We underline that the magnetic moment strongly depends on the crystal direction in which the calculations are performed (i.e., easy, intermediate, and hard magnetization axes).

2. Computational Method

For the spin-polarized first-principles electronic structure calculations at T = 0 K, we used the experimental lattice parameters reported for the $ErAl_2$ and $ErNi_2$ Laves phases **[15,16]**. The $MgCu_2$-type cubic structure (space group Fd-3m (227)) was constructed for both compounds, and the electron configurations of Al, Ni, and Er were defined as [Ne] $3s^2$ $3p^1$, [Ar] $3d^8$ $4s^2$, and [Xe] $4f^{12}$ $6s^2$, respectively. The selected lattice parameters for constructing the crystalline structures were a = b = c = 7.770 Å for $ErAl_2$ [15] and a = b = c = 7.113 Å for $ErNi_2$ [16]. The A and B atoms in the AB_2 structure occupy the 8a and 16d Wyckoff positions (i.e., at (0 0 0) and (5/8 5/8 5/8)). The ferromagnetic order for both compounds was simulated under the assumption that only the rare earth element (i.e., Er), located at the 8a site, possesses the magnetic moment, which is oriented along the <001> direction. Al and Ni, occupying the 16d Wyckoff position, were presumed to have zero magnetic moments **[11,12]**. The Erbium spin magnetic moment value was set to + 3 μ_B, while the spin magnetic moment values for Al or Ni were assigned as 0. The spin quantization axis is <001>. During energy calculations, there were neither any constraints on crystal (volume is fully relaxed) nor on magnetic structures considering. Figure 1(a) illustrates the crystal structure exhibiting ferromagnetic order used for collinear spin-polarized quantum simulations. The easy magnetization direction corresponds to the crystalline direction in the <111>-axis for $ErAl_2$ [26] and in the <001>-axis for $ErNi_2$ **[16,27,28]**. For $ErAl_2$, our calculations were performed along the hard magnetization axis (i.e., the c-axis) [27].

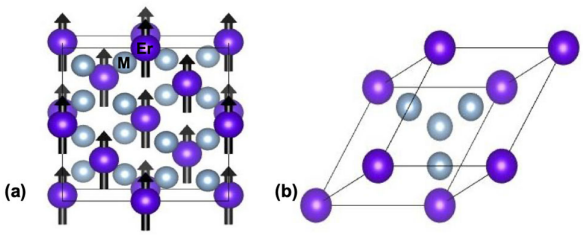

Figure 1. Schematic representation of the cubic $MgCu_2$-type crystal structure (a) and its primitive cell (b) for the ferromagnetically ordered ErM_2 Laves phases with M = Al and Ni. Purple and grey spheres represent Er and M atoms, respectively; the arrow in the purple spheres represents the magnetic moment of the rare earth element.

The geometric optimization of the crystalline structures of $ErAl_2$ and $ErNi_2$ Laves phases was performed using the Broyden–Fletcher–Goldfarb–Shanno (BFGS) algorithm **[29,30]**. The primitive cell (i.e., rhombohedral trigonal with lattice parameters a = b = c and angles $\alpha = \beta = \gamma = 60^o$) of the ErM_2 (M = Al, Ni) crystal structure, depicted in Figure 1(b), was used for energy calculations. During

 doi:10.20944/preprints202505.0871.v1

the geometric optimization process, external compressive stress was applied along the a, b, and c axes, which are perpendicular to the yz, xz, and xy atomic planes, respectively. This external stress is equivalent to applying hydrostatic pressure P. The diagonal components of the stress tensor $\sigma_{ij} = -P\,\delta_{ij}$, where P is the hydrostatic pressure, and δ_{ij} is the Kronecker delta. The bulk modulus B and its derivative were obtained by fitting the calculated third-order Birch-Murnaghan equation of state.

Spin-polarized calculations were done using the revised Perdew-Burke-Ernzerhof (RPBE) exchange-correlation functional within a Generalized Gradient Approximation (GGA) framework. To determine the electronic density of states (DOS), the Brillouin zone was integrated using a *k*-mesh of 13 × 13 × 13. A cutoff energy of 500 eV was applied for plane-wave propagation through the crystal structure **[31–34]**. The charge convergence for self-consistent field cycles was set at 1×10^{-6} eV. The GGA method alone is inadequate for describing the localized 4f and itinerant 3d electrons; thus, the Hubbard parameter U was introduced to model the ferromagnetic ordering of these 4f and 3d electrons **[18,35,36]**. The U values for localized electrons were 2.50 eV for Ni atoms and 6.0 eV for Er atoms. The U value due to the lack of localized electrons was set to 0 eV for Al atoms. It is crucial to emphasize that U corrections within the GGA framework have shown better accuracy than other LDA or hybrid functionals for investigating the magnetic behavior and electronic structure of 4f and 3d compounds **[18,35–38]**. All calculations were performed along the <001> axis using density functional theory with U corrections (DFT+U) implemented in the Cambridge Serial Total Energy Package (CASTEP) code [32].

3. Results and Discussion

3.1. Electronic Structure at Normal Pressure

Figures 2(a) and **2(b)** illustrate the calculated density of states (DOS) for $ErAl_2$ and $ErNi_2$ without hydrostatic pressure. In both cases, the s and p orbitals are localized in deeper energy zones (with peak energy values of around – 47 and – 22 eV, respectively), and their DOS is almost symmetric in shape (as shown in more detail in **Figure 3**). Notice in **Figure 3** the unfolding of the asymmetric p orbitals when Ni replaces Al in the C15-type crystal structure, which evidences the effect of substituting the post-transition metal (Al) with the transition metal (Ni). The electronic states corresponding to the electrons in s orbitals lie at ($E - E_F$) energies between – 50 and – 45 eV, while those in p orbitals are at $-25 < E - E_F < -20$ eV. The latter indicates that in the ferromagnetically ordered $ErAl_2$ and $ErNi_2$ Laves phases, the p electrons contribute minimally to the net magnetic moment. In contrast, the d and f orbitals are localized around the Fermi energy level ($E - E_F = 0$ eV), and exhibit strong hybridization that significantly influences the magnetic moment.

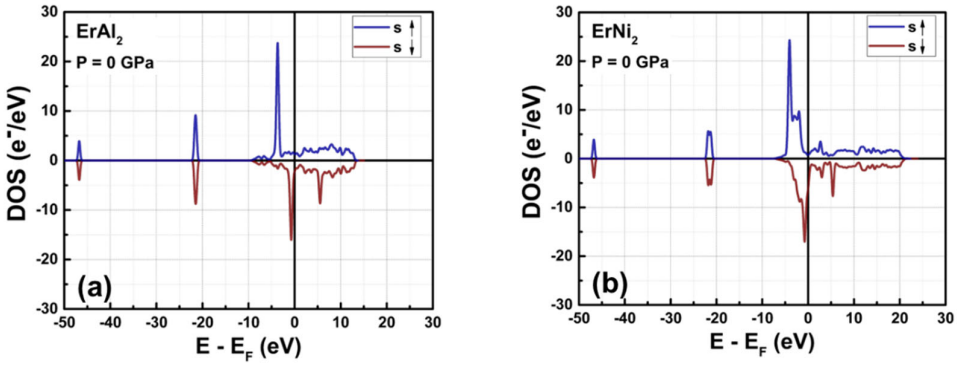

Figure 2. Calculated total density of states (DOS) at P = 0 GPa for $ErAl_2$ (**a**) and $ErNi_2$ (**b**) Laves phases. The Fermi level, indicated by the vertical solid line, is set to 0 eV.

For $ErAl_2$, the spin-up and spin-down DOS profiles of d orbitals show remarkable symmetry, like to that of the s and p orbitals. This symmetry explains their minimal contribution to the total magnetic moment, as **Figure 2(a)** illustrates. Conversely, **Figure 2(b)** shows that in $ErNi_2$, the spin-

 doi:10.20944/preprints202505.0871.v1

polarized DOS profiles of d and f orbitals are highly asymmetric, highlighting their significant role in the material's magnetic behavior. This also indicates that the hybridization between electrons in these two orbitals is more substantial for this compound than for $ErAl_2$, which has fewer unpaired d electrons than $ErNi_2$. The hybridization of d and f orbitals occurs at energies near the Fermi level (i.e., in the $-10 < E - E_F < 0$ eV range).

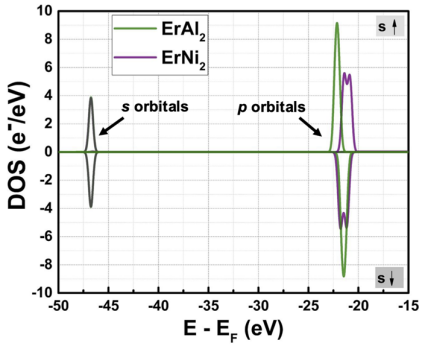

Figure 3. Calculated partial DOS at P = 0 GPa for the $ErAl_2$ and $ErNi_2$ Laves phases.

Table 1 shows the total magnetic moment value obtained through DOS for the $ErAl_2$ and $ErNi_2$ Laves phases. To determine the net magnetic moment, we used the following expression:

$$\mu_T = \int_{E_1}^{E_F} n_{S\uparrow}(E)\,dE - \int_{E_2}^{E_F} n_{S\downarrow}(E)\,dE \quad (1)$$

where E_1 and E_2 denote the energies of the electronic states with up and down spins, respectively [39]. The saturated magnetic moment obtained was 4.40 μ_B/f.u. for $ErAl_2$ and 5.56 μ_B/f.u. for $ErNi_2$. From these magnetic moment values, the estimated saturation magnetization is approximately 111 Am^2/kg for $ErAl_2$ and 109 Am^2/kg for $ErNi_2$, both of which align with the experimental values at T = 2 K and $\mu_0 H = 5$ T reported in the scientific literature for polycrystalline samples [15,16].

Table 1. Magnetic moment values obtained from the calculated DOS using eq. (1), the spin-polarized electron numbers of $n_{S\uparrow}$ and $n_{S\downarrow}$, and the electronic state difference $\Delta n(E_F)$ at the Fermi level determined for the ferromagnetic Laves phases $ErAl_2$ and $ErNi_2$ along the <001> axis.

Compound	$n_{S\uparrow}(E_F)$ (e^-/eV)	$n_{S\downarrow}(E_F)$ (e^-/eV)	$\Delta n(E_F)$ (e^-/eV)	$\mu_{S\uparrow}$ (μ_B/f.u.)[15,16	$\mu_{S\downarrow}$ (μ_B/f.u.)	μ_T^{DFT+U} (μ_B/f.u.)	μ_T^{Exp} (μ_B/f.u.)	Magnetization axis	reference
$ErAl_2$	1.31	– 2.24	– 0.93	30.19	– 25.80	4.40	**4.40** **4.75** †	**hard**	**[40]** **[26]**
$ErNi_2$	0.78	– 6.20	– 5.42	36.46	– 30.40	5.56	**5.30** ‡ **6.23**	**easy**	**[27]** **[40]**

† Single crystal with T_C = 14 K [26]; ‡ Single crystal with T_C = 7 K [27].

For $ErAl_2$, the DFT values correspond to a spontaneous magnetic moment of zero internal magnetic field (4.20 μ_B/f.u.) along the <001> hard magnetization direction in single crystals *[26,40]*. The obtained value (4.40 μ_B/f.u. at T = 0 K) is consistent with the reported spontaneous magnetic moment (4.20 μ_B/f.u. at T = 4.2 K) by Purwins et al. *[26,40]*, extrapolated from an intermediate magnetic field to the zero internal magnetic field (from 0 T to 8 T). At high magnetic fields (from 10 T to 14 T), the saturation magnetic moment rises to 5.3 μ_B/f.u. in a single crystal *[26,40]*.

Detailed experimental magnetic measurements by Gignoux and Givord [27] for the $ErNi_2$ single crystal at T = 1.5 K reported a spontaneous magnetic moment of 5.0 μ_B/f.u. at $\mu_0 H = 0$ T along the <001> easy magnetization axis. The extrapolated magnetic moment is 5.3 μ_B/f.u. at zero internal magnetic field. Consequently, when the magnetic field increases to 13 T, the saturation magnetic

 doi:10.20944/preprints202505.0871.v1

moment rises slowly and nearly linearly to 5.9 μ_B/f.u. Our spontaneous magnetic moment calculated through DFT+U is 5.56 μ_B/f.u. at T = 0 K and agrees with the magnetic experiments along the <001> easy magnetization axis in $ErNi_2$.

Figures 4(a) and **4(b)** illustrate the partial density of states (PDOS) for the d and f orbitals of both compounds, calculated without considering hybridization. **Figure 4(a)** shows that the shape of the d orbitals changes from symmetrical to slightly asymmetrical in their spin-polarized DOS profile, leading to an increase in electron populations per state when the post-transition metal (Al) is replaced by the transition metal (Ni). The maximum $n(E_F)$ value for the d orbitals increases from 0.38 e^-/eV in $ErAl_2$ to 9.13 e^-/eV in $ErNi_2$. Consequently, hybridization between the d and f orbitals occurs in the crystal structure of $ErNi_2$. In contrast, in $ErAl_2$ the Al atoms lack unpaired electrons in the d orbitals; therefore, the d and f orbitals are distinguished in the electronic structure, as depicted in **Figures 2(a)** and **4(b)**. This behavior results in a reduced contribution of electrons localized in the d orbitals to the net magnetic moment in the electronic structure of $ErAl_2$ compared to that of $ErNi_2$, as shown in **Table 2**. It is remarkable to note that for both alloys in the spin-up channels, the 4f electrons of rare earth elements are far from the Fermi level, located at – 3.41 eV ($ErAl_2$) and – 3.57 eV ($ErNi_2$). In contrast, the spin-down channels of the 4f bands are close to the Fermi level, and for both compounds they are located at – 0.74 eV; see **Figure 4(b)** for more details. **Figure 4(a)** illustrates the 4d and 3d bands of Er atoms in $ErAl_2$, which are localized from – 1.8 eV to the Fermi level; while the 3d bands corresponding Ni atoms are the majority electronic states compared the states of 4d and 3d bands of Er atoms in $ErNi_2$, as illustrates the **Figure 4(a)**. They are localized between – 5 eV and 0 eV for both spin-up and spin-down branches in $ErNi_2$. The hybridization in $ErNi_2$ basically comes from 3d and 4f states. The contribution of d electrons is nearly negligible for $ErAl_2$, while 32 % of the net magnetic moment in $ErNi_2$ arises from d electrons, as illustrated in **Figures 2(b)** and **4(a)**. For the $ErAl_2$ and $ErNi_2$ compounds, the f orbitals are the most populated, providing the most significant contribution to the net magnetic moment.

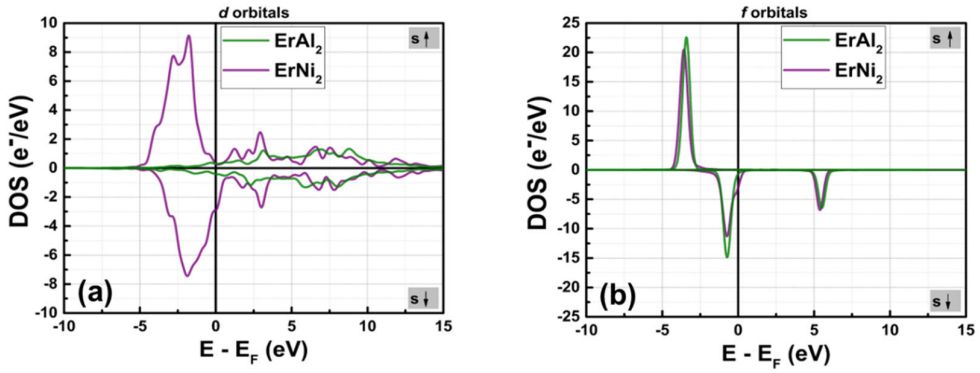

Figure 4. Calculated partial electronic DOS for orbitals d (**a**) and f (**b**) in the $ErAl_2$ and $ErNi_2$ Laves phases.

Table 2 illustrates the contribution of various orbitals to the net magnetic moment per formula unit (f.u.) derived from partial electronic density of states (DOS) calculations. The magnetic moment value is negative for electrons localized in the s, p, and d orbitals in $ErAl_2$, indicating that the magnetic moment is oriented opposite to the applied field (which aligns with the spin-up band orientation). A similar situation occurs for $ErNi_2$, where the magnetic moments of the s and p electrons are also oriented against the applied field. On one hand, the high symmetry of the electronic structure of the s and p electrons results in a minimal contribution to the net magnetic moment. On the other hand, the asymmetry in the spin-polarized partial DOS of f-electrons in $ErAl_2$ is responsible for the elevated magnetic moment. The asymmetry in the partial DOS for $ErNi_2$, observed in both the d and f electrons, contributes to a substantial magnetic moment.

 doi:10.20944/preprints202505.0871.v1

Table 2. Magnetic moment values of the s, p, d, and f orbitals determined from PDOS calculations for $ErAl_2$ and $ErNi_2$ Laves phases.

Laves phase	μ^s (μ_B/f.u.)	μ^p (μ_B/f.u.)	μ^d (μ_B/f.u.)	μ^f (μ_B/f.u.)	μ_T (μ_B/f.u.)
$ErAl_2$	– 0.005	– 0.002	– 0.001	4.940	4.932
$ErNi_2$	– 0.058	– 0.249	1.737	4.701	6.131

3.2. Electronic Structure at Moderate Hydrostatic Pressures

Figures 5(a) to **5(d)** show the calculated density of states (DOS) for the ferromagnetic ground state of $ErAl_2$ and $ErNi_2$ Laves phases under external hydrostatic pressures ranging from 0 GPa to 1.0 GPa. First, it is essential to note that the s and p orbitals remain nearly symmetric across all hydrostatic pressures and exhibit low electronic occupation compared to the d and f orbitals (refer to **Figures 6(a)** to **6(d)** for additional details on the partial density of states, PDOS). Conversely, in both compounds, the p electronic bands are more responsive to pressure than the s bands, shifting slightly toward higher energies while maintaining their symmetric behavior. The electronic population is redistributed per eV for the p and f electronic bands. In both $ErAl_2$ and $ErNi_2$, the s bands maintain their shape. In contrast, the p band in $ErAl_2$ splits into a double peak at P = 1.0 GPa, whereas in $ErNi_2$, a double peak is observed within the range of 0 GPa ≤ P ≤ 1.0 GPa. At P = 1.0 GPa, $ErNi_2$ exhibits a double peak for the spin-up p-band, while the spin-down p-band remains nearly a single peak. Notably, f orbitals are the most electronically populated within the studied pressure range. They shift far from the Fermi level while retaining their asymmetry in the DOS profile as the pressure approaches to 0.9 GPa in $ErAl_2$. Conversely, in $ErNi_2$, the f, d, and p orbitals start to disrupt the DOS symmetry at 1.0 GPa (with each spin-up band shifting to higher energy and the spin-down band remaining at lower energy), as shown in **Figure 5(d)**. This indicates the presence of Pauli paramagnetism, which stems from the shift of the spin-up band relative to the spin-down band. When the external hydrostatic pressure rises to 1 GPa, the spin-up 4f bands in $ErAl_2$ alloy move significantly away from the Fermi level compared to P = 0 GPa. They shift from – 3.41 eV at 0 GPa to – 3.95 eV at 1 GPa for spin-up bands and from – 0.74 eV at 0 GPa to – 1.55 eV at 1 GPa for spin-down bands, as illustrated in **Figure 6(b)**. Conversely, the 4f bands for the $ErNi_2$ alloy shifted closer to the Fermi level for both spin-up and spin-down branches at pressures up to 0.9 GPa. An exception occurs at an external pressure of 1 GPa, where the band splits into several others; see **Figure 6(d)**. **Figure 6(a)** shows that in $ErAl_2$, the 4d and 3d bands move closer to the Fermi level as the applied external pressures increase to 1 GPa, reaching – 1.33 eV and – 0.98 eV for the bottom of the spin-up and spin-down branches, respectively. The same occurs for both spin-up and spin-down Ni 3d bands (most electronic states) of $ErNi_2$; they move closer to the Fermi level when the applied external pressure increases from 0 GPa to 1 GPa, as shown in **Figure 6(c)**.

 doi:10.20944/preprints202505.0871.v1

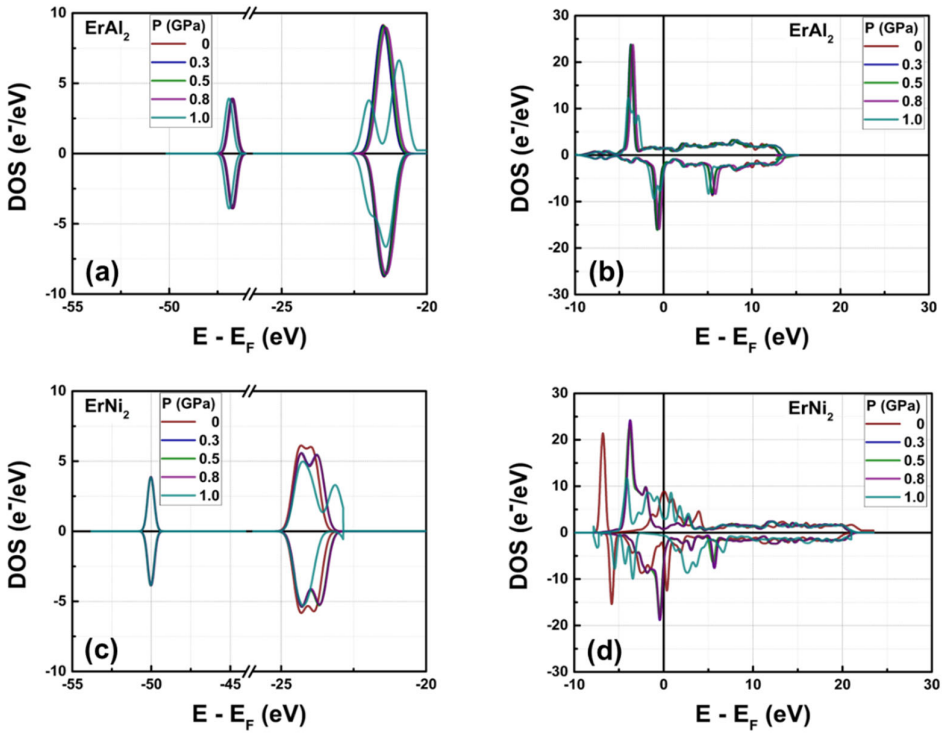

Figure 5. Effect of hydrostatic pressure on the calculated total density of states (DOS) in $ErAl_2$ [(**a**) s and p orbitals, and (**b**) hybridized d-f orbitals], and $ErNi_2$ [(**c**) s and p orbitals, and (**d**) hybridized d-f orbitals].

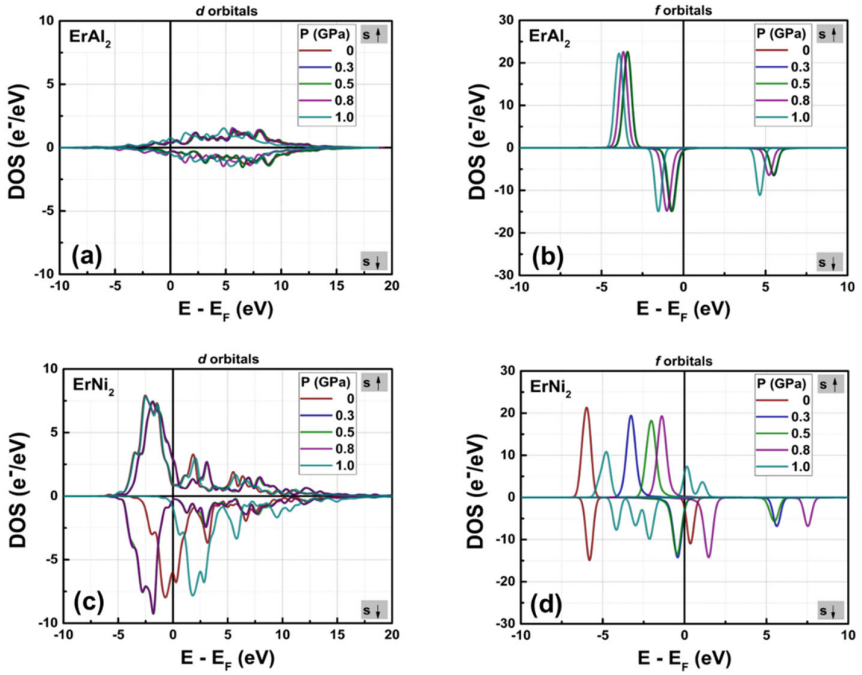

Figure 6. Evolution of the calculated partial DOS with the applied hydrostatic pressure (0 GPa ≤ P ≤ 1.0 GPa) for the d and f orbitals in $ErAl_2$ [(**a**) and (**b**)] and in $ErNi_2$ [(**c**) and (**d**)] compounds.

Figure 7(a) illustrates the relationship between the total magnetic moment and the applied hydrostatic pressure for the $ErAl_2$ and $ErNi_2$ Laves phases. Notably, up to 1.0 GPa, the calculated magnetic moment for the ferromagnetic $ErAl_2$ and $ErNi_2$ Laves phases remains nearly constant, with mean values of 4.33 μ_B/f.u. for $ErAl_2$ and 5.73 μ_B/f.u. for $ErNi_2$. **Figure 7(b)** illustrates how the contributions of electrons from the d and f orbitals to the net magnetic moment vary with pressure

 doi:10.20944/preprints202505.0871.v1

in both compounds. In $ErAl_2$, the electrons localized in the f orbitals account for nearly the entire net atomic magnetic moment across the full pressure range. The contribution from electrons localized in the d orbitals decreases dramatically to zero as the external hydrostatic pressure reaches 1.0 GPa. As a result, the electrons in the f orbitals are the main contributors to the total magnetic moment in the ferromagnetic $ErNi_2$ Laves phase.

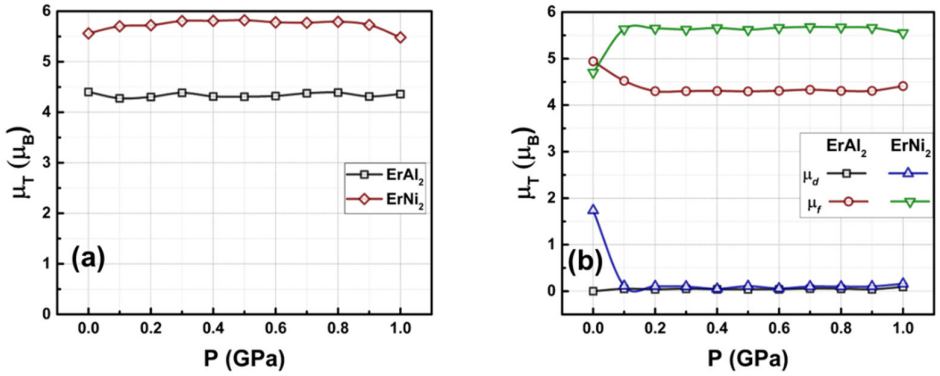

Figure 7. Total magnetic moment (**a**) and magnetic moment per d and f orbitals (**b**) as a function of the applied hydrostatic pressure (0 GPa ≤ P ≤ 1.0 GPa) for the $ErAl_2$ and $ErNi_2$ Laves phases.

The formation energy for the two studied Laves phases as a function of the applied hydrostatic pressure P, within the range of 0 GPa ≤ P ≤ 1.0 GPa, is illustrated in **Figure 8**. As indicated by the figure, the stability of the crystalline structures $ErAl_2$ and $ErNi_2$ remains unaffected by the external hydrostatic pressures applied. The formation energy, E_f, is approximately -1.04×10^4 eV for $ErAl_2$ and -1.44×10^4 eV for $ErNi_2$. The primitive cubic lattice parameter, obtained from geometric optimization, decreases from $a_0 = 5.555$ Å at 0 GPa to 5.526 Å at 1.0 GPa for $ErAl_2$. In comparison, the lattice parameter for $ErNi_2$ decreases from $a_0 = 5.103$ Å at 0 GPa to 5.085 Å as the pressure increases from 0 to 1.0 GPa. The relative compressive stress caused by this lattice reduction can be calculated using $\Delta = (V_P - V_0) / V_0 \times 100$ %, where ΔV is the volume difference $V_P - V_0$. Δ reaches values of – 1.56 % and – 1.01 % at P = 1.0 GPa for $ErAl_2$ and $ErNi_2$, respectively. **Table 3** summarizes the compressive stress values in the crystal structure up to 1.0 GPa and the bulk modulus B, which slightly increase with the hydrostatic pressure dependence and the stress tensor diagonal component σ_{ij} (i = j = 1, 2, 3). The mean value of $ErNi_2$ bulk modulus (<B> ≈ 131 GPa) is almost twice as large as that of $ErAl_2$ bulk moduli (<B> ≈ 66 GPa), see **Table 3**. As previously mentioned, based on pressure spin-polarization DFT calculations, the cubic crystalline structures remain stable within the applied range of compressive stress.

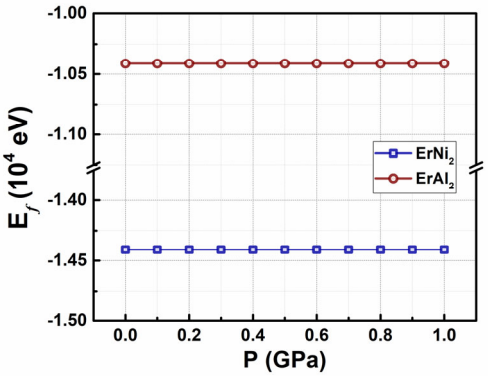

Figure 8. Formation energy as a function of applied hydrostatic pressure (0 GPa ≤ P ≤ 1.0 GPa) for the two studied Laves phases.

 doi:10.20944/preprints202505.0871.v1

In $ErAl_2$ and $ErNi_2$, the $d_{Al\text{-}Al}$ and $d_{Ni\text{-}Ni}$ interatomic distances (between two Al or Ni atoms) decrease by 0.54 % and 0.35 % under an applied pressure of 1 GPa (see **Table 3**). Concurrently, the interatomic distances $d_{Er\text{-}Al}$ and $d_{Er\text{-}Ni}$ (between Er atoms and Al or Ni atoms) diminish by 0.52 % and 0.33 %, respectively. Note that $ErAl_2$ exhibits greater sensitivity to pressure than the $ErNi_2$ alloy. The interatomic distances change very little with the applied pressure for both Laves phases. This maintains the same ferromagnetic environment for each atom, with only the electronic states adjusting due to the applied hydrostatic pressure. Consequently, the values of the saturation spontaneous magnetic moment remain nearly constant for each Laves phase.

Table 3. Unit cell volume (V_P) of the rhombohedral trigonal structure, bulk modulus B, the diagonal component σ_{ij} of the stress tensor, and compressive stress (Δ) as a function of the applied hydrostatic pressure for the $ErAl_2$ and $ErNi_2$ phases (0.0 GPa ≤ P ≤ 1.0 GPa).

Alloy	**$ErAl_2$**							**$ErNi_2$**						
P (GPa)	**a (Å)**	**$d_{Al\text{-}Al}$ (Å)**	**$d_{Er\text{-}Al}$ (Å)**	**V_P (Å³)**	**Δ (%)**	**B (GPa)**	**σ_{ij} (GPa)**	**a (Å)**	**$d_{Ni\text{-}Ni}$ (Å)**	**$d_{Er\text{-}Ni}$ (Å)**	**V_P (Å³)**	**Δ (%)**	**B (GPa)**	**σ_{ij} (GPa)**
0.0	5.5551	2.777	3.257	121.218	0.000	63.76	−0.00184	5.1030	2.551	2.991	93.949	0.000	128.13	−0.00631
0.1	5.5530	2.776	3.256	121.090	−0.105	64.53	−0.06960	5.1023	2.550	2.990	93.853	−0.101	128.56	−0.10767
0.2	5.5503	2.775	3.254	120.908	−0.255	64.87	−0.16420	5.1010	2.549	2.989	93.737	−0.225	129.90	−0.22623
0.3	5.5455	2.772	3.251	120.590	−0.517	65.76	−0.31888	5.0999	2.548	2.988	93.653	−0.314	129.89	−0.31054
0.4	5.5434	2.771	3.250	120.456	−0.628	65.96	−0.38991	5.0973	2.547	2.987	93.560	−0.413	130.11	−0.40776
0.5	5.5412	2.770	3.249	120.310	−0.748	66.14	−0.47108	5.0956	2.546	2.986	93.464	−0.516	130.82	−0.50732
0.6	5.5374	2.768	3.247	120.062	−0.953	66.98	−0.59076	5.0939	2.546	2.985	93.366	−0.620	131.39	−0.61002
0.7	5.5345	2.767	3.245	119.873	−1.108	67.08	−0.69311	5.0921	2.545	2.984	93.270	−0.722	131.91	−0.71256
0.8	5.5315	2.765	3.243	119.677	−1.270	67.56	−0.79821	5.0904	2.544	2.983	93.182	−0.816	132.08	−0.80705
0.9	5.5275	2.763	3.242	119.324	−1.561	67.96	−0.88224	5.0888	2.543	2.982	93.102	−0.901	132.88	−0.89113
1.0	5.5259	2.762	3.240	119.318	−1.566	68.04	−0.99389	5.0853	2.542	2.981	92.994	−1.015	133.12	−1.00668

3.3. Determination of Electronic Coefficient in Specific Heat Capacity

From metals theory, in the absence of hydrostatic pressure, the Fermi energy E_F at $T = 0$ K can be calculated as

$$E_F = \frac{h^2 {k_B}^2}{2 m_e} \left(\frac{3 N}{8 \pi V} \right)^{2/3} \quad (2)$$

 doi:10.20944/preprints202505.0871.v1

where N/V represents the electron density and m_e is the mass of the electron. If one atom contributes one electron to the Fermi gas in the solid, the $ErAl_2$ and $ErNi_2$ compounds exhibit electron densities N/V of 1.687×10^{28} m^3 and 2.208×10^{28} m^3, respectively (assuming mass densities of 6.20×10^3 kg/m^3 [13,41] and 10.44×10^3 kg/m^3 [42], along with molar masses of 221.223 g mol^{-1} and 216.468 g mol^{-1}, respectively). Our calculations of the Fermi energy E_F and the temperature $T_F = E_F/k_B$ at T = 0 K yield 2.401 eV and 2.788×10^4 K for $ErAl_2$, and 2.873 eV and 3.336×10^4 K for $ErNi_2$. The obtained values align with those reported for other pure metals such as Al (18.1×10^{28} m^3, 11.7 eV, 13.6×10^4 K), Au (5.9×10^{28} m^3, 5.55 eV, 6.43×10^4 K), and Na (2.65×10^{28} m^3, 3.26 eV, 3.78×10^4 K), among others [43]. Thus, the electronic or Sommerfeld coefficient can be calculated using the following formula:

$$\gamma_e = \frac{\pi^2 \, {k_B}^2 \, N_A}{3 \, E_F} = \frac{\pi^2 \, k_B \, N_A}{3 \, T_F} \tag{3}$$

where N_A is the Avogadro constant. The obtained γ_e values from equation (3) are 1.470×10^{-3} J mol^{-1} K^{-2} for $ErAl_2$ and 1.229×10^{-3} J mol^{-1} K^{-2} for $ErNi_2$.

Based on the DFT simulations, we can also calculate the γ_e coefficient for metals and alloys using the Einstein-Debye model:

$$c_p(T) = \gamma_e \, T + \beta_{ph} \, T^3 \tag{4}$$

where $c_{p,e} = \gamma_e \, T$ and $c_{p,ph} = \beta_{ph} \, T^3$ denote the electronic and phonon contributions to the specific heat capacity at constant pressure.

In the low-temperature limit (that is, far from the Debye temperature, i.e., $T \ll T_D$), the electronic coefficient γ_e in the Sommerfeld approximation can be correlated with the electronic density of states $\Delta n(E_F)$ at the Fermi level [39] using the expression:

$$\gamma_e = \frac{\pi^2 \, {k_B}^2}{3} \Delta n(E_F) \tag{5}$$

where k_B is the Boltzmann constant. This expression remains valid within the framework of hydrostatic pressure. **Figure 9** presents the results obtained from DFT calculations using Eq. (5) for the electronic specific heat coefficient of both alloys. At P = 0 GPa, the γ_e coefficient for $ErAl_2$ is 2.1×10^3 J mol^{-1} K^{-2}, which is in reasonable agreement with previous values calculated from the electron gas model in metals (i.e., 1.470×10^{-3} J mol^{-1} K^{-2}). In contrast, the γ_e coefficient for $ErNi_2$ at P = 0 GPa reaches 13.0×10^{-3} J mol^{-1} K^{-2}, almost ten times the value obtained from the electron gas model (i.e., 1.229×10^{-3} J mol^{-1} K^{-2}). As shown in **Figure 9,** the γ_e coefficient remains nearly constant for both alloys up to a hydrostatic pressure of 1.0 GPa.

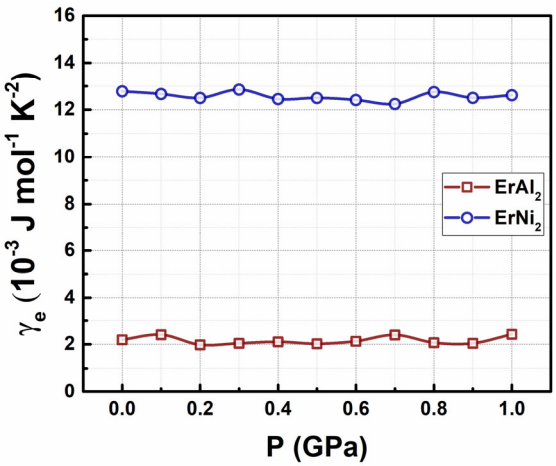

Figure 9. Electronic specific heat coefficient as a function of the hydrostatic pressures up to P = 1.0 GPa for $ErAl_2$ and $ErNi_2$ Laves phases.

 doi:10.20944/preprints202505.0871.v1

4. Conclusions

Through DFT calculations utilizing the revised Perdew-Burke-Ernzerhof (RPBE) exchange-correlation functional within a Generalized Gradient Approximation (GGA) framework and incorporating Hubbard U correction, we investigated the effects of hydrostatic pressure of up to 1.0 GPa on the stability of the crystal structure, as well as on the electronic and magnetic properties of the cubic Laves phases $ErAl_2$ and $ErNi_2$. The main findings can be summarized as follows: (a) The net spontaneous magnetic moment per formula unit remained constant throughout the entire pressure range considered, with values of 4.40 μ_B/f.u. for $ErAl_2$ along the <001> hard magnetization axis and 5.56 μ_B/f.u. for $ErNi_2$ along the <001> easy magnetization axis. (b) The cubic $MgCu_2$-type crystal structure retains its stability up to 1 GPa. At this pressure, the compressive stress affecting the crystalline structure is – 1.56 % for $ErAl_2$ and – 1.01 % for $ErNi_2$. The interatomic distances change very little with the applied pressure, which keeps virtually the same ferromagnetic environment for each atom, while a rearrangement of the electronic states (mainly in the f, d, and p orbitals) occurs due to the applied hydrostatic pressure. (c) The electronic contribution to the specific heat aligns in order of magnitude with the anticipated data from the metal gas model and remains stable up to 1.0 GPa. (d) The d-f hybridization lowers electronic states and diminishes the spontaneous magnetic moments.

Author Contributions: Conceptualization, T.L.S. and C.F.S.V.; methodology, T.L.S. and C.F.S.V..; software, T.L.S.; validation, T.L.S., J.L.E.C. and C.F.S.V.; formal analysis, T.L.S., J.L.E.C. and C.F.S.V.; investigation, T.L.S., J.L.E.C., J.L.S.LL. and C.F.S.V.; resources, J.L.S.LL and C.F.S.V.; data curation, T.L.S. and C.F.S.V.; writing—original draft preparation, T.L.S. and C.F.S.V.; writing—review and editing, T.L.S., J.L.S.LL., J.L.E.C. and C.F.S.V.; visualization, J.L.S.LL. C.F.S.V.; supervision, C.F.S.V.; project administration, J.L.S.LL; funding acquisition, J.L.S.LL and C.F.S.V. All authors have read and agreed to the published version of the manuscript.

Funding: This research was funded by CONAHCyT, under the research project CF-2023-I-2143 and CBF-2025-G1263.

Data Availability Statement: The data supporting this study's findings are available from the corresponding author upon reasonable request.

Acknowledgments: This work was supported by CONAHCyT, México, under the research projects CF-2023-I-2143 and CBF-2025-G1263 and Laboratorio Nacional de Nanociencias y Nanotecnología (LINAN, IPICyT). The authors thank Universidad Autónoma de Ciudad Juárez for providing BIOVIA Materials Studio software licensing to perform materials science modeling and simulations. T. López-Solenzal thanks the financial support from CONAHCyT, México, for his PhD studies. C.F. Sánchez-Valdés acknowledges the support from IIT-UACJ for his research activities.

Conflicts of Interest: The authors declare that they have no known competing financial interests or personal relationships that could have appeared to influence the work reported in this paper.

References

1. Pecharsky, V.K.; Gschneider Jr., K.A. Magnetocaloric effect and magnetic refrigeration. *J. Magn. Magn. Mater.* **1999**, *200*, 044-56. DOI: https://doi.org/10.1016/S0304-8853(99)00397-2.
2. Moya, X.; Mathur, N.D. Caloric materials for cooling and heating. *Science.* **2020**, *370*, 797–803. DOI: https://doi.org/10.1126/science.abb0973.
3. Moya, X.; Kar-Narayan, S.; Mathur, N.D. Caloric materials near ferroic phase transitions. *Nature Mater.* **2014**; *14*, 439-450. DOI: https://doi.org/10.1038/nmat3951.
4. Franco, V.; Blázquez, J.S.; Ipus, J.J.; Law, J.Y.; Moreno-Ramírez, L.M.; Conde A. Magnetocaloric effect: From materials research to refrigeration devices. *Prog. Mater. Sci.* **2018**, *93*, 112-232. DOI: https://doi.org/10.1016/j.pmatsci.2017.10.005.

 doi:10.20944/preprints202505.0871.v1

5. Tang, X.; Sepehri-Amin, H.; Terada, N.; Martin-Cid, A.; Kurniawan, I.; Kobayashi, S.; Kotani, Y.; Takeya, H.; Lai, J.; Matsushita, Y.; Ohkubo, T.; Miura, Y.; Nakamura, T.; Hono, K. Magnetic refrigeration material operating at a full temperature range required for hydrogen liquefaction. *Nature Comm*. **2022**, *13*, 1817. DOI: https://doi.org/10.1038/s41467-022-29340-2.
6. Smith, A.; Bahl, C.R.H.; Bjørk, R.; Engelbrecht, K.; Nielsen, K.K.; Pryds, N. Materials challenges for high performance magnetocaloric refrigeration devices. *Adv. Energy Mater.* **2012**, *2*, 1288-1318. DOI: https://doi.org/10.1002/aenm.201200167.
7. Pecharsky, V.K.; Gschneidner Jr., K.A. Giant magnetocaloric effect in $Gd_5(Si_2Ge_2)$. *Phys. Rev. Lett.* **1997**, *78*, 4494. DOI: https://doi.org/10.1103/PhysRevLett.78.4494.
8. Kitanovski, A. Energy applications of magnetocaloric materials. *Advanced Energy Mater.* **2020**, *10*, 1903741. DOI: https://doi.org/10.1002/aenm.201903741.
9. Lyubina, J. Magnetocaloric materials for energy efficient cooling. *J. Phys. D. Appl. Phys.* **2017**, *50*, 053002. DOI: https://doi.org/10.1088/1361-6463/50/5/053002.
10. Gschneidner Jr., K.A.; Pecharsky, V.K. Binary rare earth Laves phases - an overview. *Z. Kristallogr.* **2006**, *221*, 375-38. DOI: https://doi.org/10.1524/zkri.2006.221.5-7.375.
11. Stein, F.; Leineweber. A. Laves phases: a review of their functional and structural applications and an improved fundamental understanding of stability and properties. *J. Mater. Sci.* **2021**, *56*, 5321-5427. DOI: https://doi.org/10.1007/s10853-020-05509-2
12. Liu, W.; Bykov, E.; Taskaev, S.; Bogush, M.; Khovaylo, V.; Fortunato, N.; Aubert, A.; Zhang, H.; Gottschall, T.; Wosnitza, J.; et al. A study on rare-earth Laves phases for magnetocaloric liquefaction of hydrogen. *Appl. Mat. Today*. **2022**, *29*, 101624. DOI: https://doi.org/10.1016/j.apmt.2022.101624.
13. Gschneidner, K.A. Jr; Pecharsky, V.K.; Tsokol, A.O. Recent developments in magnetocaloric materials. *Rep. Prog. Phys.* **2005**, *68*, 1479. DOI: https://doi.org/10.1088/0034-4885/68/6/R04.
14. Kumar K.S.; Hazzledine, P. M. Polytypic transformations in Laves phases. *Intermetallics*. **2004**, *12*, 763-770. DOI: https://doi.org/10.1016/j.intermet.2004.02.017.
15. Sánchez Llamazares, J.L.; Zamora, J.; Sánchez-Valdés, C.F.; Álvarez-Alonso, P. Design and fabrication of a cryogenic magnetocaloric composite by spark plasma sintering based on the RAl_2 Laves phases (R = Ho, Er). *J. Alloys Compd.* **2020**, *831*, 154779. DOI: https://doi.org/10.1016/j.jallcom.2020.154779.
16. Sánchez Llamazares, J.L.; Ibarra-Gaytán, P.; Sánchez-Valdés, C.F.; Ríos-Jara, D.; Álvarez-Alonso, P. Magnetocaloric effect in $ErNi_2$ melt-spun ribbons. *J. Rare Earths.* **2020**, *38*, 612-616. DOI: https://doi.org/10.1016/j.jre.2019.07.011.
17. Biswas, A.; Pathak, A.K.; Zarkevich, N.A.; Liu, X.; Mudryk, Y.; Balema, V.; Johnson, D.D.; Pecharsky, V.K. Designed materials with the giant magnetocaloric effect near room temperature. *Acta Materialia*. **2019**, *180*, 341-348. DOI: http://doi.org/10.1016/j.actamat.2019.09.023.
18. Hafner, J.; Wolverton, C.; Ceder, G. Toward computational materials design: the impact of density functional theory on materials research. *MRS Bulletin*. **2006**, *31*, 659-668. DOI: https://doi.org/10.1557/mrs2006.174.
19. Pan F.-Ch., Lin, X.-l.; Li J., Ma, L.; Ma, L.-C., Cheng H.M. The electronic structures and Ferromagnetism of Cu-Doped ZnO: the first-principle calculation Study. *J. Supercond. Nov. Magn.* **2018**, 31, 2103-2110. DOI: https://doi.org/10.1007/s10948-017-4417-6.
20. Patel, P.D.; Shinde, S.; Gupta, S.D. First principle calculation of structural, electronic and magnetic properties of Mn_2RhSi Heusler alloy. *AIP Conf. Proc.* **2018**, *2005*, 040004. DOI: https://doi.org/10.1063/1.5050744.
21. Wang, S. First-principles prediction of ferromagnetism in transition-metal doped monolayer AlN. *Superlattices Microstruct.* **2019**, *122*, 171-180. DOI: https://doi.org/10.1016/j.spmi.2018.08.009.

 doi:10.20944/preprints202505.0871.v1

22. Odkhuu, D.; Tsevelmaa, T.; Sangaa, D.; Tsogbadrakh, N.; Rhim, S.H.; Hong, S.C. First-principles study of magnetization reorientation and perpendicular magnetic anisotropy in $CuFe_2O_4$/MgO heterostructures. *Phys. Rev. B.* **2018**, *98*, 094408. DOI: https://doi.org/10.1103/PhysRevB.98.094408.
23. Kanomata, T.; Endo, H.; Mori, S.; Okajima, H.; Hihara, T.; Sumiyama, K.; Kaneko, T.; Suzuki, K. Specific heat of MnAlGe, MnGaGe and MnZnSb. *J. Magn. Magn. Mater.* **1995**, *140-144 Part 1*, 133-134. DOI: https://doi.org/10.1016/0304-8853(94)00832-9.
24. Aschauer, U.; Braddell, R.;. Brechbuhl, S.A; Derlet, P.M.; Spaldin, N.A. Strain-induced structural instability in FeRh. *Phys. Rev. B.* **2016**, *94*, 014109. DOI: https://doi.org/10.1103/PhysRevB.94.014109.
25. He, L.; Zhu, J.; Zhang, L. First-principles study of Structural phase transition, electronic, elastic and thermodynamic properties of C15-type Laves phases $TiCr_2$ under pressure. *Physica B: Condensed Matter.* **2018**, *531*, 79-84. DOI: https://doi.org/10.1016/j.physb.2017.11.051.
26. Purwins, H.G.; Walker, E.; Barbara, B.; Rossignol, M.F.; Furrer, A. Single crystal magnetization of $ErAl_2$ and interpretation in terms of the crystalline field. *J. Phys. C: Solid State Phys.* **1976**, 9, 1025-1030. DOI: https://doi.org/10.1088/0022-3719/9/6/019.
27. Gignoux, D.; Givord, F. Quadrupolar interactions in $ErNi_2$. *J. Magn. Magn. Mater.* **1983**, 31-34, 217-218. DOI: https://doi.org/10.1016/0304-8853(83)90222-6.
28. Ibarra-Gaytán, P.J.; Sánchez Llamazares, J.L.; Álvarez-Alonso, P.; Sánchez-Valdés, C. F.; Gorria, P.; Blanco, J.A. Magnetic entropy table-like shape in RNi_2 composites for cryogenic refrigeration. *J. Appl. Phys.* **2015**, *117*, 17C116. DOI: https://doi.org/10.1063/1.4915480.
29. Eyert, V. A comparative study on methods for convergence acceleration of iterative vector sequences. *J. Comput. Phys.* **1996**, *124*, 271-285. DOI: https://doi.org/10.1006/jcph.1996.0059.
30. Pfrommer, B. G.; Côté, M.; Louie, S.G.; Cohen, M.L. Relaxation of crystals with the quasi-Newton method. *J. Comput. Phys.* **1997**, *131*, 233-240. DOI: https://doi.org/10.1006/jcph.1996.5612.
31. Lewars, E. Computational chemistry: introduction to the theory and applications of molecular and quantum mechanics. First edition, **2004**. ISBN: 0-306-48391-2, Print ISBN: 1-4020-7285-6.
32. Clark, S.J.; Seagall, M.D.; Pickard, C.J.; Hasnip, P.J.; Probert, M.I.J.; Refson, K.; Payne, M.C. First principles methods using CASTEP. *Z. Kristallogr.* **2005**, *220*, 567-570. DOI: https://doi.org/10.1524/zkri.220.5.567.65075.
33. Bader, R.F.W. The density in density functional theory. *J. Molec. Struct.: THEOCHEM.* **2010**, *943*, 2-18. DOI: https://doi.org/10.1016/j.theochem.2009.10.022.
34. Monkhorst, H.J.; Pack, J.D. Special points for Brillouin-zone integrations, *Phys. Rev. B.* **1976**, *13*, 5188. DOI: https://doi.org/10.1103/PhysRevB.13.5188.
35. Cococcioni, M.; de Gironcoli, S. Linear response approach to the calculation of the effective interaction parameters in the LDA+U method. *Phys. Rev. B.* **2005**, 71, 035105. DOI: https://doi.org/10.1103/PhysRevB.71.035105.
36. Anisimov, V.I.; Zaanen, J.; Andersen; O.K. Band theory and Mott insulators: Hubbard *U* instead of Stoner *I*. *Phys. Rev. B.* **1991**, 44, 943. DOI: https://doi.org/10.1103/PhysRevB.44.943.
37. Moroni, E.G.; Kresse, G.; Hafner, J.; Furthmüller, J. Ultrasoft pseudopotentials applied to magnetic Fe, Co, and Ni: From atoms to solids. *Phys. Rev. B.* **1997**, 56, 15629. DOI: https://doi.org/10.1103/PhysRevB.56.15629.
38. Staroverov, V. N.; Scuseria, G. E.; Tao, J.; Perdew, J. P. Test of the ladder of density functionals for bulk solids and surfaces. Phys. Rev. B. **2004**, *69*, 075102. DOI: https://doi.org/10.1103/PhysRevB.69.075102.
39. Cyrot, M.; Lavagna, M. Density of states and magnetic properties of the rare-earth compounds RFe_2, RCo_2 and RNi_2. *Le Journal de Physique.* **1979**, *40*, 763. DOI: https://doi.org/10.1051/jphys:01979004008076300.
40. Taylor, K.N.R. Intermetallic rare-earth compounds. *Advances in Physics.* **1971**, *20*, 551-660. DOI: https://doi.org/10.1080/00018737100101311.

 doi:10.20944/preprints202505.0871.v1

41. Harris, I.R.; Mansey, R.C.; Raynor, G.V. Rare earth intermediate phases: III. The cubic laves phases formed with aluminium and cobalt. *J. Less-Common Met.* **1965**, *9*, 270-280. DOI: https://doi.org/10.1016/0022-5088(65)90020-2.
42. Gschneidner Jr., K. A.; L. Eyring. Handbook on the Physics and Chemistry of Rare Earths. Vol. 2 – Alloys and Intermetallics, North-Holland, **1978**. ISBN: 0444850228, 9780444850225.
43. Tipler, P.A.; Llewellyn, R. Modern Physics, Fifth Edition, **2008**. ISBN-13: 978-0-7167-7550-8, ISBN-10: 0-7167-7550-6.